Formation of Oligonucleotide-Gated Silica Shell-Coated Fe₃O₄-Au Core–Shell Nanotrisoctahedra for Magnetically Targeted and Near-Infrared Light-Responsive Theranostic Platform

Wei-Peng Li,[†] Pei-Yi Liao,[†] Chia-Hao Su,[‡] and Chen-Sheng Yeh*[,†]

[†]Department of Chemistry, Center for Micro/Nano Science and Technology and Advanced Optoelectronic Technology Center, National Cheng Kung University, Tainan 701, Taiwan

[‡]Center for Translational Research in Biomedical Sciences, Kaohsiung Chang Gung Memorial Hospital, Kaohsiung 833, Taiwan

Ⓢ *Supporting Information*

ABSTRACT: A new multifunctional nanoparticle to perform a near-infrared (NIR)-responsive remote control drug release behavior was designed for applications in the biomedical field. Different from the previous studies in formation of Fe₃O₄-Au core–shell nanoparticles resulting in a spherical morphology, the heterostructure with polyhedral core and shell was presented with the truncated octahedral Fe₃O₄ nanoparticle as the core over a layer of trisoctahedral Au shell. The strategy of Fe₃O₄@polymer@Au was adopted using poly-L-lysine as the mediate layer, followed by the subsequent seeded growth of Au nanoparticles to form a Au trisoctahedral shell. Fe₃O₄@Au trisoctahedra possess high-index facets of {441}. To combine photothermal and chemotherapy in a remote-control manner, the trisoctahedral core–shell Fe₃O₄@Au nanoparticles were further covered with a mesoporous silica shell, yielding Fe₃O₄@Au@mSiO₂. The bondable oligonucleotides (referred as dsDNA) were used as pore blockers of the mesoporous silica shell that allowed the controlled release, resulting in a NIR-responsive DNA-gated Fe₃O₄@Au@mSiO₂ nanocarrier. Taking advantage of the magnetism, remotely triggered drug release was facilitated by magnetic attraction accompanied by the introduction of NIR radiation. DNA-gated Fe₃O₄@Au@mSiO₂ serves as a drug control and release carrier that features functions of magnetic target, MRI diagnosis, and combination therapy through the manipulation of a magnet and a NIR laser. The results verified the significant therapeutic effects on tumors with the assistance of combination therapy consisting of magnetic guidance and remote NIR control.
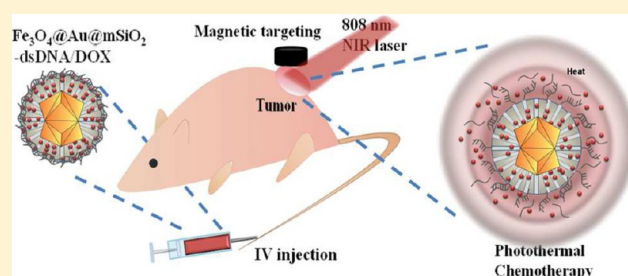
INTRODUCTION

Assembling different materials into a single nanostructure may provide superior and sometimes unprecedented properties and also offers a promising way to obtain multifunctionalities derived from each building block. Unlike single-component materials which usually contain only one unique property of the active ingredient, the ingredients of multicomponent materials determine the versatile properties and applications of these materials. From the materials point of view, fabrication of polyhedral metal or metal oxide core–shell heterostructures with polyhedral cores and shells is attractive but a challenging task. Those core–shell heterostructures with well-defined shapes are the promising catalytic and electrocatalytic candidates because of their high activity of the exposed surface planes and the synergistic effect between the shells and the incorporated metal cores. Nevertheless, the components of those heterostructures are mainly reported in the noble metals of Au, Ag, Pd, and Pt.[1−12] For example, the pioneer work reported by Yang et al. used cubic Pt cores as templates for the epitaxial growth of Pd cubes, octahedrons, and cuboctahedrons.[1] Formation of Pd or Ag nanocubes from the Au octahedral cores was performed by Tian et al.[2] The different

Au@Pd polyhedral shapes were nicely demonstrated through epitaxial growth of Pd trisoctahedral, hexoctahedral, and tetrahexahedral layers on Au trisoctahedral nanocrystals.[3] In addition, Au tetrahexahedra have been employed to direct the growth of tetrahexahedral Au@Pd.[4] Huang et al. successfully synthesized a series of polyhedral Au@Pd and Au@Ag using either cubic, octahedral, or rhombic dodecahedral Au nanocrystal cores.[5−8]

Herein, we report for the first time the synthesis of polyhedral Fe₃O₄@Au core–shell nanoparticles (NPs), a trisoctahedral shape, from truncated octahedral Fe₃O₄. Based on the reported literatures, synthetic strategies of the nanocomposite which comprise of both iron oxide and Au components to yield core–shell Fe₃O₄@Au can be generally categorized into three approaches: (1) Fe₃O₄@Au was prepared by the formation of Fe₃O₄@polymer@Au through the assistance of the mediate layer of polymer where Au seeds were grafted on a polymer shell and subsequently grew as an Au nanoshell;[13−19] (2) Fe₃O₄@Au was generated in the form

Scheme 1. Schematic Illustration of the Synthesis Process of $Fe_3O_4@Au@mSiO_2$-dsDNA/DOX Nanoparticles for Therapy Combining Chemotherapy and Photothermal Treatment of Cancer Cells *in Vivo* in a Magnetic Targeting Manner
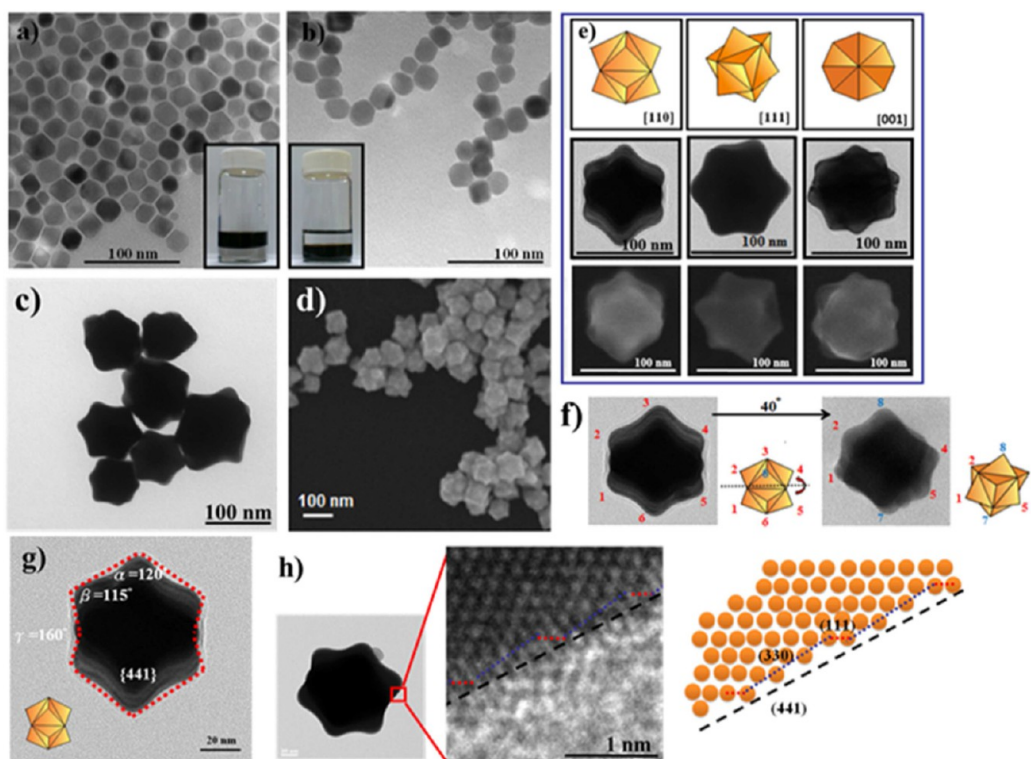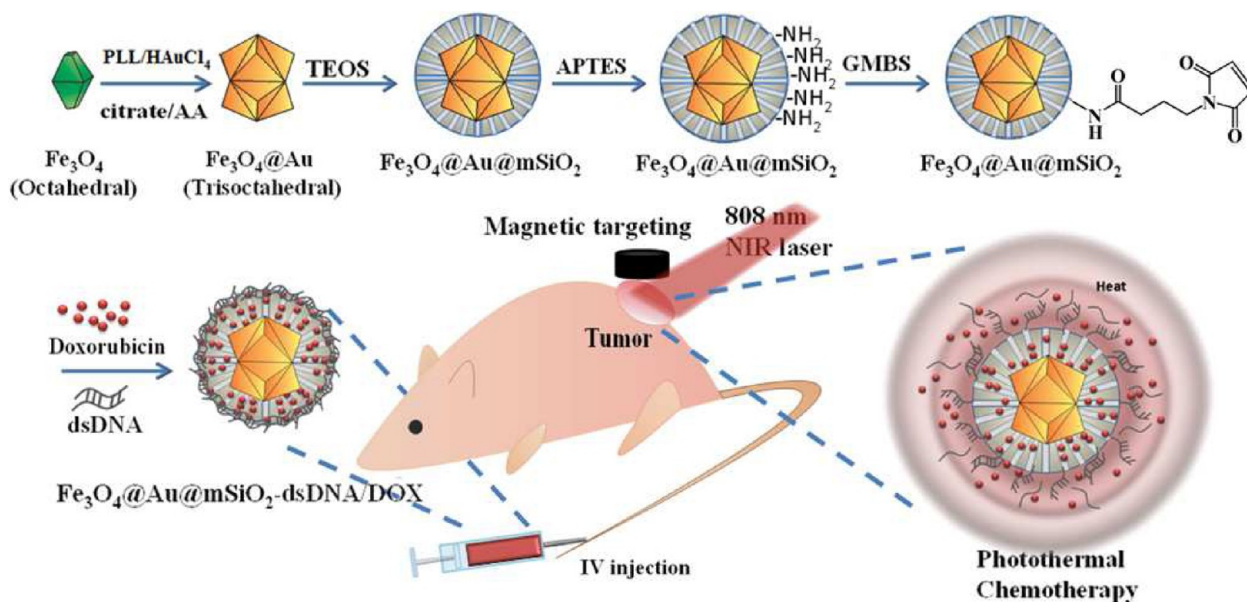

Figure 1. TEM images showed octahedral Fe_3O_4 NPs in (a) hexane and (b) deionized water; insets: iron oxide NPs were dispersed in oil phase (top) or water phase (bottom). (c) TEM image of trisoctahedral $Fe_3O_4@Au$ NPs. (d) SEM image of trisoctahedral $Fe_3O_4@Au$ NPs. (e) TEM/SEM images and corresponding geometric model of trisoctahedral $Fe_3O_4@Au$ NPs projected from different orientations. (f) TEM image of trisoctahedral $Fe_3O_4@Au$ NPs tilted by 40° from [110] to [111] projection. (g) TEM image of trisoctahedral $Fe_3O_4@Au$ NP and structural model viewed along the [110] zone axes. (h) HRTEM image of an edge-on facet showing {441} facets and the corresponding atomic model projected from the [110] direction. The {441} can be viewed as a combination of {330} and {111} subfacets.

of $Fe_3O_4@SiO2@Au$ where the silica shell over the surface of Fe_3O_4 was utilized for the seeded growth of Au NPs to form Au nanoshell;[20−22] and (3) Au^{3+} was directly reduced on the Fe_3O_4 surfaces to yield an Au deposition shell.[23−26] To date, the spherical core−shell morphology has been the common shape

for $Fe_3O_4@Au$. Mostly, the aforementioned approaches all started with spherical Fe_3O_4 cores growing Au spherical shells that exhibited a rough surface in the form of either aggregated domains or a continuous layer. Although Fe_3O_4 nanocubes have been introduced to direct the growth of $Fe_3O_4@Au$ by

Halas et al.[27] and Amal et al.,[15] the final structures again all come to spherical core−shell morphology. It remains a challenge to fabricate a Fe_3O_4@Au core−shell polyhedral structure that could potentially provide multimodal functions offered by the shell and the encapsulated core. In this study, the strategy of Fe_3O_4@polymer@Au was adopted using poly-L-lysine (PLL) as the mediate layer, followed by the subsequent seeded growth of Au NPs to form an Au trisoctahedral shell.

The development of multicomponent materials as the theranostic nanosystems has a potential to establish a new therapeutic mode giving targeted drug delivery, imaging, and a combination therapy of chemotherapy and hyperthermia, which can greatly increase therapeutic efficacy and minimize the damage to normal tissues. From the biomedicine point of view, incorporation of Au component into iron oxide NPs provides the integration of magnetic and plasmonic functions that is a novel nanomedical platform for targeted delivery and diagnostic imaging, using the magnetic property, and therapeutics, using the optical property. Formation of Au trisoctahedral nanoshell results in the surface plasmon absorption potentially shifted to the near-infrared (NIR) region, acting as NIR-responsive nanomaterials, which is not possible for the similar sizes of Au spherical and trisoctahedral NPs. For the applications in biomedicine, the as-prepared Fe_3O_4@Au trisoctahedral NPs were constructed as NIR-responsive chemo- and photothermal therapeutic agents treated in animals after systemic administration, which is different from the previous studies primarily using Fe_3O_4@Au in photothermal ablation at the cell culture level.[18,25,26,28]

Stimuli-responsive controlled-release carriers are the best choice for on-demand drug delivery platform. The drug-carrying carriers reach the lesion and release the drug carried. It helps to reduce the amount of drug needed and improve the effects of treatment. Among all, the mesoporous silica is a good choice for its high apparent volume, adjustable material size, and good biocompatibility, whereas the pores of mesoporous silica NPs are ideal for carrying drugs. Therefore, we further fabricated a mesoporous SiO_2 ($mSiO_2$) nanoshell onto the surface of Fe_3O_4@Au, yielding Fe_3O_4@Au@$mSiO_2$, to develop the multimodal nanocarriers with the combination of magnetic targeted drug delivery, MRI monitored magnetic targeting of tumor, on-demand drug release, and NIR photothermal ablation, as shown in Scheme 1, for *in vivo* therapy of cancer upon systemic administration. Iron oxide NPs are promising drug delivery vehicles effectively toward the target tissue with the use of external magnets after local administration, offering benefits beyond the enhanced permeability and retention effect. With this promising approach, formulation of an effective dosing regimen can be achieved to limit the possible systemic toxicity. This advantage comes from the property of iron oxide NPs as magnetic responsiveness.

■ RESULTS AND DISCUSSION

According to our previous study,[29] ∼22 nm-sized (length between diagonal apexes) truncated octahedral Fe_3O_4 NPs distributed in hexane were produced with thermally decomposed iron acetylacetonate, $Fe(acac)_3$, containing oleic acid and trioctylamine (Figure 1a). Figure 2a shows that the representative 22 nm-sized magnetite exhibits a truncated rhombohedral shape consisting of (111) and (001) faces in the [110] projection. The projected shape was a truncated square shape taken from the zone axis [001] (Figure 2b). These results show that the NPs exhibit a truncated octahedron. The
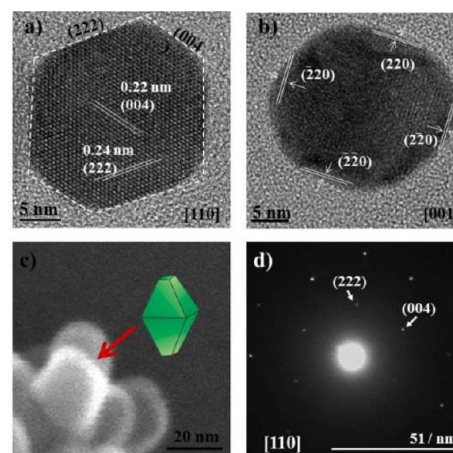

Figure 2. HR-TEM image of a truncated octahedral magnetite NP (∼22 nm in diagonal apexes) taken along with (a) [110] zone axis and (b) [001] zone axis. (c) SEM image of a truncated octahedral Fe_3O_4 NP (red arrow) corresponding to the geometric model in a [110] orientation. (d) The electron diffraction pattern of a [110]-oriented truncated octahedral Fe_3O_4 NP.

scanning electron microscope (SEM) image shows a type of octahedral structure (Figure 2c). The electron diffraction pattern of a single [110]-oriented NP provides a more detailed analysis of 22 nm-sized NPs, through Fe_3O_4 diffraction spots generated (Figure 2d). Ligand exchange was introduced to add hydrophilic polymer of COOH-PEG-COOH on the iron oxide surface. Figure 1b provides the transmission electron microscopy (TEM) of iron oxide distributed in deionized water. Next was the attempt to coat the iron oxide particle with a gold shell. The positively charged PLL (M_W:1000−5000) was selected to modify the negative surface charge of iron oxide NPs, providing the amine groups needed to capture citrate-coated Au seeds. Au seeds were synthesized in a $HAuCl_4$ solution at pH 10.9 with trisodium citrate. In such an alkaline environment, the seeds grew quickly to 1−2 nm and were deposited on the surface of iron oxides. Subsequently, L-ascorbic acid (AA) was used for the seed growth to generate the gold shell on the surface of iron oxides (Fe_3O_4@Au NPs).

One interesting observation in the growth of Au nanoshell is the transformation in structure. Our results shown in the electron microscopy image suggest that the Au shell was not a spherical structure. Instead, it was an Au nanoshell with a polyhedral structure (Figure 1c,d). The particle size was 100 nm estimated from the diagonal apexes (a core of 22 nm and a shell of 39 nm in thickness). A subsequent high-resolution analysis was performed on the single particle (Figure 1e), showing [110], [111], and [001] projected orientations with good consistency between the geometrical model of the trisoctahedral structure and the electron microscopy images (TEM and SEM). Figure 1f shows that the tilt analysis of high-resolution TEM (HR-TEM) started from the projection direction of [110] along the dash line and turned 40°, resulting in the project direction to become close to [111]. It was found that the angles seventh and eighth positions that did not show in the project direction of [110] appeared after a turn of 40°, which proved that this was a good trisoctahedral structure. To further identify the facets of poly structure NPs, the Miller indices of high-index facets were defined as the projection angles of the selected crystallographic directions. Table S1 suggests that the projection angles of the projection direction
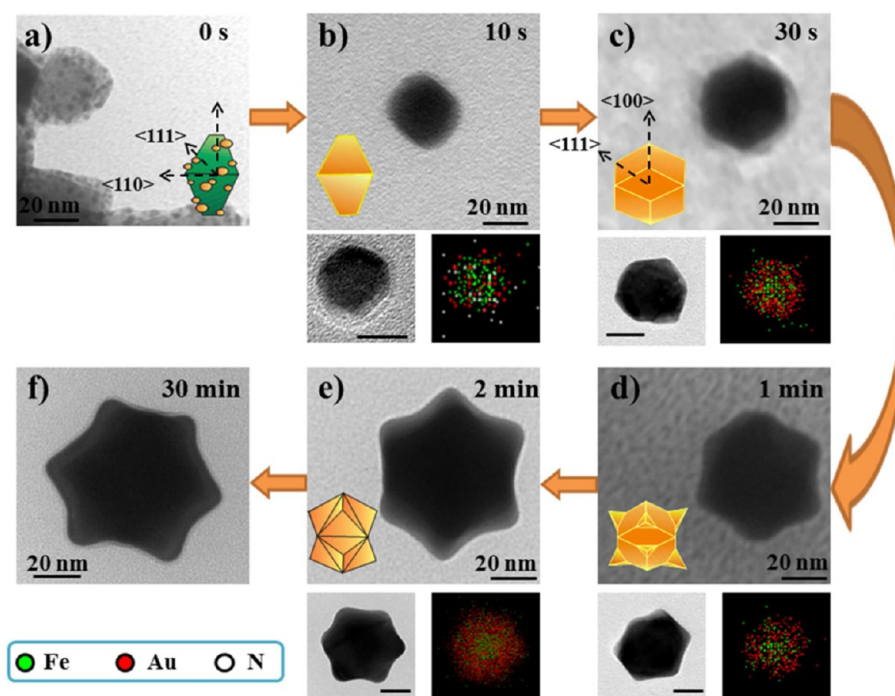
Figure 3. TEM images with element analysis (spot-mapping) and corresponding geometric models of NPs observed with different reaction times: (a) 0, (b) 10, (c) 30 s, (d) 1, (e) 2, and (f) 30 min. The color was selected for the indicated elements on EDS (green spot: iron, red spot: gold, white spot: nitrogen).

[110] of trisoctahedron correspond to the Miller indices of high-index facets on an ideal crystalline model. Figure 1g shows that at the projection direction [110], the angles of α, β, and γ were measured 120°, 115°, and 160°, respectively, which verified that this trisoctahedron consists of high-index facets of {441}. HRTEM image showing stepped facets indicates that the {441} facet projected from [110] zone axis is multiply stepped and is composed of {330} and {111} subfacets (Figure 1h).

To understand the structural evolution in formation of trisoctahedral Fe_3O_4@Au, the TEM images and energy dispersive spectroscopy (EDS) were studied at different reaction times along the process (Figure 3). Before AA was added at time 0, the Fe_3O_4 NPs were observed to have many Au seeds adsorbed on their surface. This was because Au seeds grew rapidly in the alkaline reactive environment and the affinity was strong between the PLL-modified iron oxide and the Au seeds. As the seed growth reached the 10 s, the size of NPs increased to ~30 nm, and presumably a thin layer of Au shell had grown on the surface. The elemental analysis indicates iron signals along with Au signals, which appeared at the outer layer. In the images, a low-contrast layer of gel-like substance was also seen coating the particles, which was suspected to be PLL adsorbed on the surface of the Au shell during the reaction and acted as the morphological control agent in the subsequent reactions. The elemental analysis suggests the presence of signals of nitrogen atom, proving that the outer layer was likely adsorbed with PLL. As time reached 30 s (Figure 3c), the dodecahedron grown across the octahedron ⟨111⟩ was detected with a hexagonal shape. The elemental analysis shows strong Au signals. At 1 min, triangular cones were growing on the high-reactive vertex angles along the ⟨111⟩ direction of Au dodecahedrons (Figure 3d). As time approached 2 min, the cones continued to grow and started connecting with one another to form the trisoctahedral Au shell (Figure 3e). Once

again, the Au signals were verified to be localized on the outer layer. When the reaction extended to 30 min (Figure 3f), no change was observed in the structure of NPs. In order to inspect the role of PLL in the formation of core−shell structure, PLL changed from a molecular weight (M_W) of 1000−5000 to 500−2000. It turned out that the trisoctahedral Fe_3O_4@Au NPs can be synthesized using PLL with M_W of 500−2000 as well (Figures 4a). To understand the relationship between the PLL structure and the growth of Au shell, an attempt was made by selecting polyethylenimine (PEI: containing only secondary amine), poly-L-histidine (PLH: with the primary amine of PLL switching to histidine groups) and poly-L-arginine (PLA: with the primary amine of PLL switching to diaminomethylidene
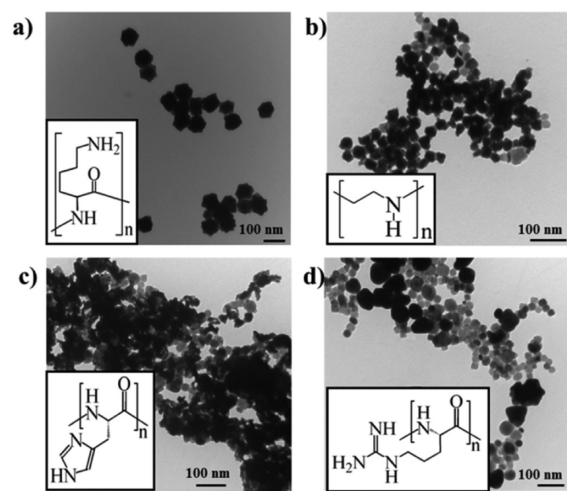

Figure 4. TEM images show the resulting NPs where the original PLL (M_W: 1000−5000) was replaced with (a) smaller PLL (M_W: 500−2000), (b) PEI, (c) PLH, and (d) PLA.

amino groups) in place of PLL. It was found that no Fe$_3$O$_4$@ Au core−shell NPs were formed here, but the individual Fe$_3$O$_4$ and Au NPs appeared in the form of aggregation (Figures 4b−d). Contrary to the observation using PLL before addition of AA at time 0 as seen in Figure 3a, we observed no Au seeds adsorbed on the surface of the Fe$_3$O$_4$ NPs in the cases of PEI and PLA from TEM images (Figure S1a,b). Although Au seeds can be seen on Fe$_3$O$_4$@PLH NPs, the degree of amount is much less than that of Fe$_3$O$_4$@PLL NPs (Figure S1c). The surface charges of those polymer-coated Fe$_3$O$_4$ NPs were then inspected by ζ potential measurements and determined them as 44.1, 25.2, 7.5, and 7.1 mV for Fe$_3$O$_4$@PLL, Fe$_3$O$_4$@PLH, Fe$_3$O$_4$@PEI, and Fe$_3$O$_4$@PLA, respectively, which shows the highest positive surface charge in Fe$_3$O$_4$@PLL. We speculate that the degree of the surface charge may strongly influence the adsorption of Au seeds. Negative citrate-coated Au seeds favor surfaces with high positive charge, like PLL, leading to Au layer formation. The lattice parameters (a) are 8.35 and 4.08 Å for Fe$_3$O$_4$ with a cubic structure and Au in a face-centered cubic structure, respectively. The lattice mismatch is 2.2% by a double of 4.08 Å (Au) with respect to 8.35 Å (Fe$_3$O$_4$). Once the Au seeds were deposited on the Fe$_3$O$_4$ surface, epitaxial growth of Au shell is likely to occur on the Fe$_3$O$_4$ core for this heterogeneous core−shell nanostructure.

Figure S2 shows diffraction signals of Fe$_3$O$_4$ and Fe$_3$O$_4$@Au NPs in X-ray diffraction (XRD) analysis. The diffraction pattern of Fe$_3$O$_4$ is consistent with the diffraction peaks of the crystalline cubic inverse spinel of bulk Fe$_3$O$_4$ (JCPDS no. 19-0629). For Fe$_3$O$_4$@Au, the strong Au peaks, which are Au fcc signals (JCPDS no. 4-0784), appear in the absence of Fe$_3$O$_4$ signal due to the 39 nm thickness of Au coating on the surface of Fe$_3$O$_4$. Superconducting quantum interference device (SQUID) analysis features the saturation magnetization (Ms) of 80 emu/g for Fe$_3$O$_4$ NPs, whereas Fe$_3$O$_4$@Au NPs dropped to 20 emu/g because of the covering of the Au shell (Figure S3). Both Fe$_3$O$_4$ and Fe$_3$O$_4$@Au NPs showed signs of remnant magnetization (B_R) at 1.1 and 0.6 emu/g, respectively, and coercivity (H_c) at 0.013 kOe and 0.012 kOe, respectively. The small remnant magnetization values may be caused by the presence of the metal Fe° showing as (110) reflection peak, as seen in the XRD spectrum of Figure S2a, resulting in the hysteresis and suggesting a ferromagnetism-like property.[29] The colloidal solutions of Fe$_3$O$_4$ and Fe$_3$O$_4$@Au NPs can be easily accumulated on the wall of the tube by the attraction of an external magnet. With the removal of the magnet attraction and the use of sonication process, the dispersed colloidal solution was obtained again (Figure S3).

As to the fabrication of Fe$_3$O$_4$@Au@mSiO$_2$ as nanocarriers, formation of the mSiO$_2$ shell over Fe$_3$O$_4$@Au also has allowed us to build up a NIR-driven gated nanocontainer (Scheme 1). To provide better therapeutic performance as the drug-loaded mesoporous silica nanomaterial reaches the target location, it is necessary to minimize or even eliminate the possibility that the drug is released into the surrounding environment in a nontherapeutic circumstance. An efficient design for the controlled drug release is that a substance is made into a cap for the pores in order to cap the pores and to keep the drugs carried in the pores from being accidentally released into the surrounding environment. With appropriate external stimulation, the cap displays the behavior of switching on/off as a control means to release the drugs contained in the pores of mesoporous silica NPs. As compared to inorganic materials and organic molecules as gatekeepers,[30−38] biomolecules provide a

basis giving biocompatibility with minimal toxicity to surrounding normal tissue and better cellular uptake to efficient intracellular drug release. We employed the double-stranded complementary oligonucleotides (referred as dsDNAs) to tether on mesopore openings to encapsulate the anticancer doxorubicin (DOX) drug as the controlled-release platforms of the dsDNA-capped Fe$_3$O$_4$@Au@mSiO$_2$. Upon heating dsDNA-capped Fe$_3$O$_4$@Au@mSiO$_2$ NPs by NIR light irradiation, the duplex DNAs unwind, eventually uncapping of pores to release guest molecules. Photo-irradiation can be an effective strategy as it is capable of accurately determining when and where to release. It is also important to select the appropriate wave band of light source. NIR light features low energy absorption to blood and soft tissues in a biological body, and, therefore, is suitable for photocontrolled drug release and photothermal treatment of deeper lesions. The Fe$_3$O$_4$@Au@ mSiO$_2$ hybrid NPs in this study provided dual therapeutic functionalities for photothermal ablation treatment as well as the chemotherapy through the remotely NIR-triggered drug release by means of the photothermal conversion of the Au nanoshell, which induced dehybridization of the complementary DNA duplexes and allowed drugs to release. Taking advantage of the magnetism of Fe$_3$O$_4$, remotely triggered intracellular anticancer drug release was facilitated by magnetic attraction as well.

To formulate the mSiO$_2$-coated drug carrier as Fe$_3$O$_4$@Au@ mSiO$_2$, Fe$_3$O$_4$@Au NPs were mixed with water solution of CTAB at 55 °C. NaOH was then added to create an environment for hydrolysis, followed by addition of TEOS, enabling the mSiO$_2$ shell to cover the surface of NPs. Figure 5a shows that the shell formed was 20 nm in thickness with pores clearly seen on the SiO$_2$ shell. The hydrodynamic diameter was determined as 149.9 nm by dynamic light scattering (DLS) (Figure S4a). The thickness of this shell is controllable by manipulating the content of TEOS in the reaction. A single NP was collected for EDS analysis (line-scan using TEM) for
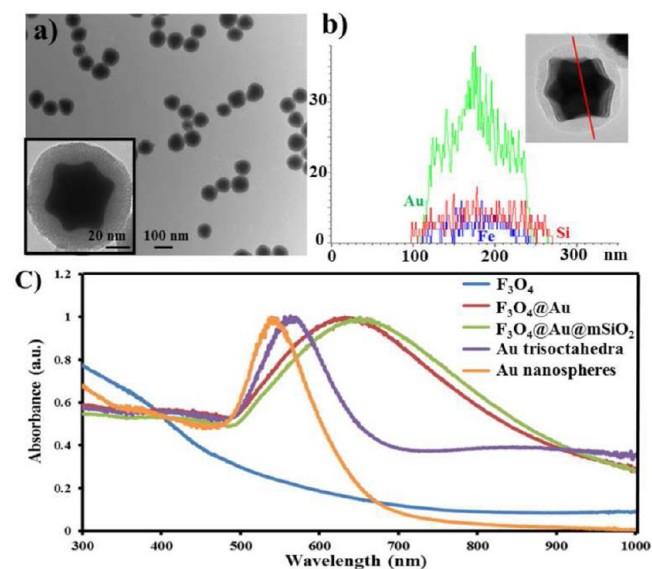
Figure 5. (a) TEM image of Fe$_3$O$_4$@Au@mSiO2 NPs (inset: magnified TEM image of a single Fe$_3$O$_4$@Au@mSiO$_2$). (b) Element analysis (line-scan) of Fe$_3$O$_4$@Au@mSiO$_2$ NPs (inset: the red line shows the path of electron beam during the line-scan). (c) UV−vis absorption spectra of the Fe$_3$O$_4$, Fe$_3$O$_4$@Au, Fe$_3$O$_4$@Au@mSiO$_2$, Au trisoctahedra, and Au nanospheres colloidal solutions.

chemical composition (Figure 5b). Elemental line-scan analysis using TEM shows clearly the distribution of iron, gold, and silicon. The element iron was concentrated at the center of the particle, followed by the strong Au signal, and the Si signal spikes were found on the outer layer, indicating that the $mSiO_2$ shell had covered the Fe_3O_4@Au NP entirely. Brunauer−Emmett−Teller (BET) was used to verify that the porous SiO_2 shell was mesoporous (Figure S5). The pores were 3 nm in size with a total surface area of 122.2 m^2/g. When the pores of Fe_3O_4@Au@$mSiO_2$ were loaded with anticancer drug, DOX, the Barrett−Joyner−Halenda (BJH) results showed that the pore volume reduced from 0.11 to 0.05 cm^3/g due to the adsorption of drugs in the pores. For comparative purposes, the similar size of Au nanospheres[39] (∼103 nm in diameter, Figure S6) and Au trisoctahedra[40] (∼104 nm in diagonal apexes, Figure S7) was synthesized along with Fe_3O_4@Au trisoctahedra to inspect the UV−vis spectral behavior. Au trisoctahedra possess the angles of α, β, and γ as 141°, 91° and 141°, giving high-index facets of {221} that consists of {111} and {110} subfacets. Electron diffraction measurements indicate that Au nanosphere and trisoctahedron all are the single crystalline. Figure 5c provides the UV−vis absorption spectra of the Au nanospheres, Au trisoctahedra Fe_3O_4, Fe_3O_4@Au, and Fe_3O_4@Au@$mSiO_2$ NPs dispersed in H_2O. Au nanospheres and trisoctahedra peak at 540 and 570 nm, respectively. As the Au trisoctahedral shell grows, the surface plasmon absorption band extends from 500 nm to 500−900 nm in the NIR wavelength range. This gives the trisoctahedral Fe_3O_4@Au as a potential NIR-responsive NPs. As the SiO_2 shell formed, a slight red shift was observed in this absorption peak.

A further modification was made to outside of the pores by designing the double-stranded dsDNAs as a cap. In order to covalently immobilize dsDNAs onto the SiO_2 surface, 3-aminopropyl-ethoxysilane (APTES) was added to react with the silanol groups of the $mSiO_2$ and thus was tethered to the SiO_2 surface. Next, N-γ-maleimidobutyryloxy succinimide (GMBS) was selected as a bridging molecule to conjugate amine groups of APTES and thiol groups of thiolated duplex DNAs. Figure S8 provides the FT-IR analysis spectra of three different modification stages, Fe_3O_4@Au@$mSiO_2$, Fe_3O_4@Au@$mSiO_2$-APTES, and Fe_3O_4@Au@$mSiO_2$-APTES-GMBS. The spectra suggest that Fe_3O_4@Au@$mSiO_2$ featured the OH bending signal from Si−OH at 1620 cm^{-1}. The functional group of −NH_2 was exposed to the material after the $mSiO_2$ shell was modified with APTES. The stretching signal of −NH was found at 1545 cm^{-1} in the figure, which proved that the APTES was modified onto the mesopous SiO_2 shell. After the modification of GMBS, the C=O stretching signal from maleimide was observed at 1660 cm^{-1}.

Prior to grafting dsDNAs to SiO_2 surface, the dsDNA was obtained from the hybridization of ssDNA with SH-5′-$(CH_2)_6$-TTTTTCCCGCGCCGG sequence and the cDNA of 5′-TTTTTCCGGCGCGGG in 4 °C phosphate buffered saline (PBS) buffer. By using a fluorescence-based method, we calculated the quantity of dsDNAs attached to NP. FAM-labeled DNA (FAM: 6-carboxy-fluorescine) was selected for quantification of dsDNAs. The self-complementary dsDNAs (SH-5′-$(CH_2)_6$-TTTTTCCCGCGCCGG and FAM-5′-TTTTTCCGGCGCGGG) were anchored on the SiO_2 surface. The amount of dsDNAs was measured from the decrease in fluorescence intensity of FAM-labeled DNAs in the supernatant with the calibration curve. It was estimated that there were ∼12830 dsDNAs on a single Fe_3O_4@Au@$mSiO_2$-dsDNA NP.

The hydrodynamic diameter of Fe_3O_4@Au@$mSiO_2$-dsDNA NPs was determined as 161.9 nm by DLS (Figure S4b). In this study, we selected anticancer drug DOX as a guest drug. The DOX was mixed with Fe_3O_4@Au@$mSiO_2$-APTES-GMBS NPs, followed by conjugation of thiolated dsDNAs in PBS buffer solution. The excess DOX was removed by centrifugation and a wash step (at least three times). The encapsulated amount of DOX was estimated to be ∼5.7 × 10^5 DOX molecules, derived from the difference in fluorescence intensity of DOX between the initial amount and residue in supernatants and calculated based on a calibration curve according to DOX concentration. Both Fe_3O_4@Au@$mSiO_2$-dsDNA and Fe_3O_4@Au@$mSiO_2$-dsDNA/DOX NPs were investigated for stability in the dark under PBS buffer at 37 °C (Figure S9). The FAM-labeled DNAs were used to monitor the stability and showed a stable hybridization with only ∼6.8% liberated DNAs after 72h. Twelve percent (12%) DOX leached in the initial 12 h, thereafter no more apparent release was noticed. In comparison, encapsulated DOX was nearly (∼99%) washed out after repeated wash four times for the DOX-loaded Fe_3O_4@Au@$mSiO_2$ in the absence of end-capping dsDNA. The present Fe_3O_4@Au@$mSiO_2$-dsDNA provides effective retention of the guest molecule. Finally, to verify the stability of NPs, we dispersed Fe_3O_4@Au@$mSiO_2$-dsDNA in PBS solutions of pH 7 and 5, cell culture Dulbecco's modified Eagle's medium (DMEM), and serum. PBS at pH 7 mimicked the extracellular environment, while PBS at pH 5 was used to examine the intracellular endosome/lysosome environment. The observation suggested that NPs remained stable and with no degradation of silica shell for 7 days (Figure S10).

The strong absorption property in the NIR band was verified on the performance of the photothermal effect on Fe_3O_4@Au and Fe_3O_4@Au@$mSiO_2$-dsDNA/DOX NPs using an 808 nm diode laser at 3 W/cm^2 (Figure S11). A thermocouple was used to measure the bulk solution temperature. The temperature of the solution rose rapidly in the initial 5 min, and leveled off after 6 min. With the increase of particle concentration, the temperature rise became more significantly for both samples. The increased temperature (>45 °C) was observed in 10 min of exposure when the particle concentration was greater than 300 ppm (of Au ion concentration). Next, laser illumination was conducted on the Fe_3O_4@Au@$mSiO_2$-dsDNA/DOX to demonstrate NIR light-controlled drug release (Figure S12). The colloidal samples with 400 ppm of Au ion concentration were added in a culture disk to be illuminated at 3W/cm^2 for 10 min, followed by being off the illumination for 5 min for the consecutive laser ON-OFF sequence. The denaturing temperature of the present dsDNAs was approximately 47 °C. A pulsatile DOX release was obtained, which demonstrated precise control of the drug release. As expected, the rapid drug release was set off by the laser illumination that caused dsDNAs to dehybridize and detach from the surface, thus leaving the drugs free to leave the pores. No distinct DOX release was detected when laser was turned off.

For *in vitro* studies, HeLa cells (human cervical cancer cell lines) were selected as the cell model. Prior to further evaluating the therapeutic efficacy, MTT assay was conducted to determine that the NPs are biocompatible to cells. Cells were cultured in culturing media with Fe_3O_4@Au@$mSiO_2$-dsDNA/DOX containing 0, 10, 50, 100, 200, and 400 ppm (of Au ion concentration) at 37 °C for 24 h. No significant cellular toxicity was detected with at least 90% of cell survival found in higher NPs concentration (Figure S13). This suggests that,
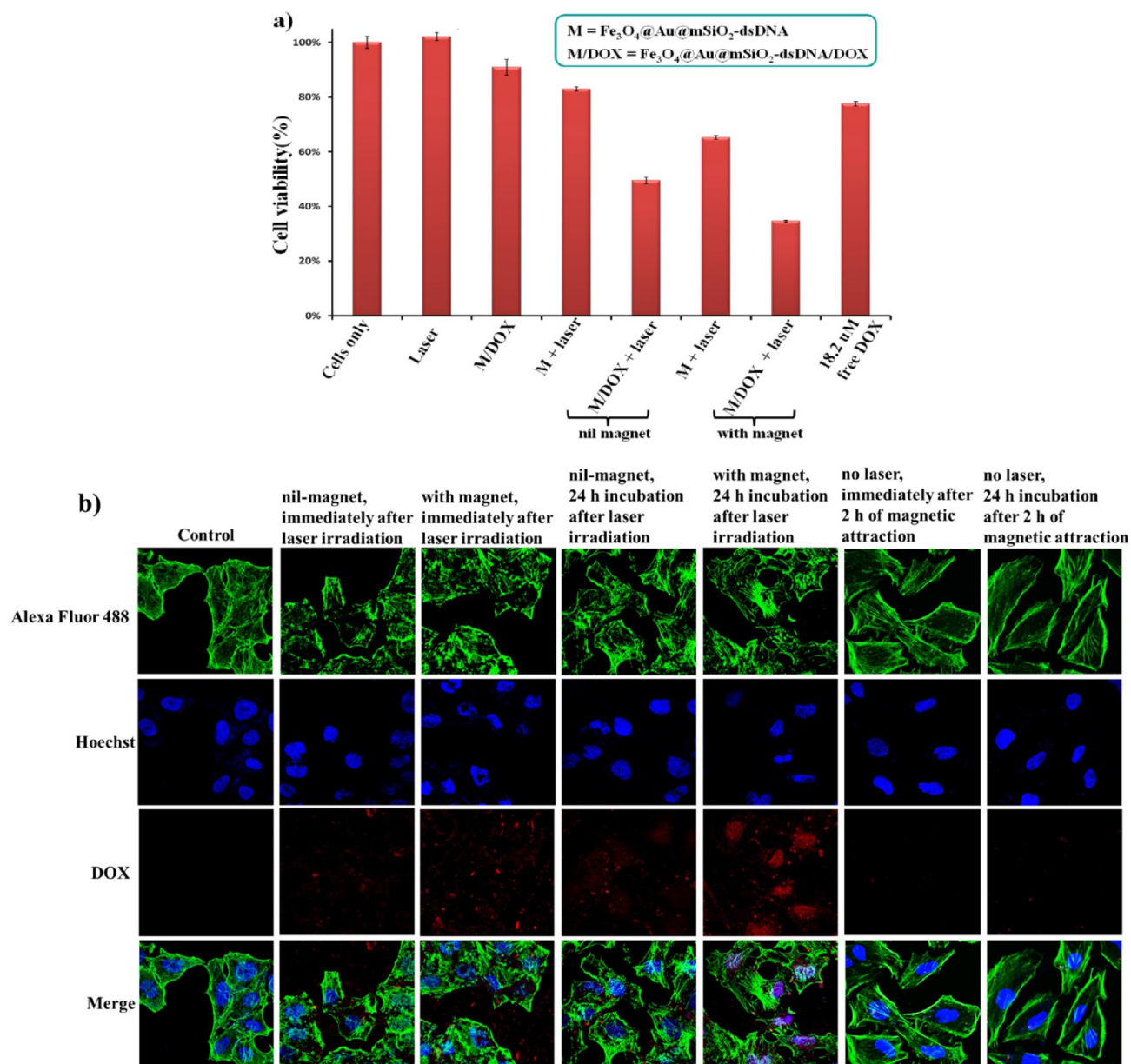
10067

dx.doi.org/10.1021/ja504118q | *J. Am. Chem. Soc.* 2014, 136, 10062−10075

Figure 6. (a) Cytotoxicity assays of HeLa cells in the presence of PBS, PBS upon NIR laser irradiation, M/DOX, M upon NIR laser irradiation, M/DOX upon NIR laser irradiation, M upon NIR irradiation with magnet attraction, M/DOX upon NIR laser irradiation with magnet attraction, and the equivalent free DOX that carried by M/DOX (M: Fe_3O_4@Au@mSiO$_2$-dsDNA, M/DOX: Fe_3O_4@Au@mSiO$_2$-dsDNA/DOX). (b) The confocal microscope images of HeLa cells were taken in the presence of PBS, and Fe_3O_4@Au@mSiO$_2$-dsDNA/DOX upon laser irradiation with/without magnet attraction, where the images were observed immediately or additional incubation for 24 h after laser irradiation. For an additional 24 h incubation period, the cells were first incubated with NPs for 2 h with or without magnetic attraction, followed by a wash process to remove uninternalized NPs. To demonstrate DOX release controlled by laser illumination, the images of HeLa cells were taken in the presence of Fe_3O_4@Au@mSiO2-dsDNA/DOX with magnet attraction in the absence of laser illumination, where the images were observed immediately or additional incubation for 24 h after 2 h of magnetic attraction. To obtain a fluorescent presentation, the cells were co-stained using fluorescent probes such as Hoechst (blue fluorescence, cell nuclei) and Alexa 488 (green fluorescence, cytoskeleton). The red fluorescent was observed from DOX. NIR illumination was performed for 10 min exposure using an 808 nm diode laser at 3W/cm^2. The magnet was applied with 2 h of magnetic attraction.

without exposure to laser illumination, Fe_3O_4@Au@mSiO$_2$-dsDNA/DOX NPs showed no apparent chemotherapeutic effect in 24 h incubation. Because the magnetic properties made the iron oxide NPs easily susceptible to manipulation by magnet attraction, the NPs with 400 ppm (of Au concentration) were fed to HeLa cells in two groups of culture dishes, wherein one was applied with magnetic attraction and the other was not. The Au content in the cells was measured after 2 h of culturing. Accordingly, the group without magnetic attraction

indicated only 150 ppm (37.5%) of Au concentration uptake to the cells. On the other hand, the proportion of Au content detected from the cells increased to 256 ppm (63.8%) in the group under magnetic attraction for 2 h, indicating that the magnetic attraction caused more cell-uptake of NPs. Subsequently, cell toxicity was examined to compare the effects of the NPs on the HeLa cells with respect to laser treatment with or without magnetic attraction. The cells were first incubated with NPs for 2 h with or without magnetic attraction, followed
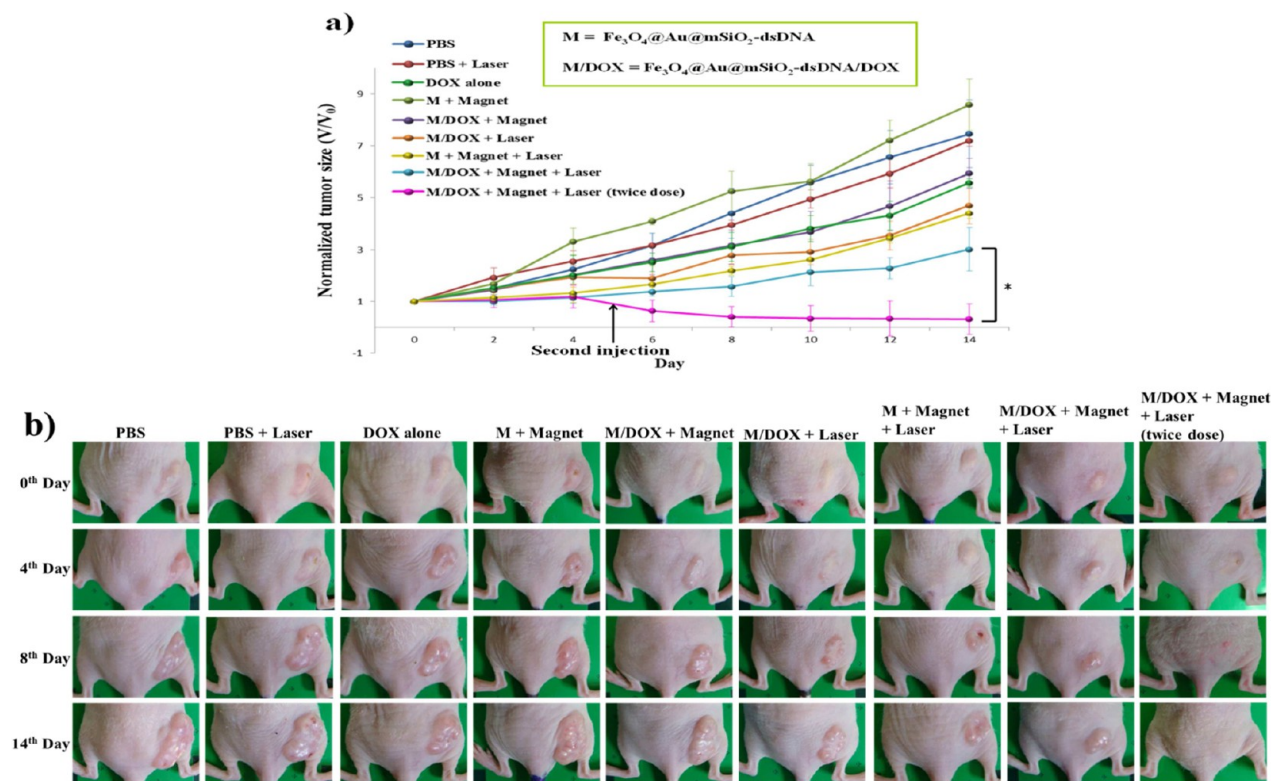
Figure 7. (a) Tumor growth curves of different treatment groups. Tumor sizes were normalized to their initial sizes (n = 5), *p < 0.05 calculated and compared to once and twice dosed group. (b) The photographs of mice after treatments at different dates. NIR illumination was performed for 30 min exposure using an 808 nm diode laser at 3 W/cm^2. The magnet was applied with 30 min of magnetic attraction.

by a wash process to remove uninternalized NPs, and then for additional 24 h incubation period (Figure 6a). In the control groups (cells only or cells + laser illumination), no significant cell death was observed. The cells treated with 400 ppm (of Au concentration) of Fe$_3$O$_4$@Au@mSiO$_2$-dsDNA/DOX but without laser illumination reached 90% of cell survival rate, which is consistent with the observation in Figure S13. The groups in the absence of magnetic attraction for Fe$_3$O$_4$@Au@mSiO$_2$-dsDNA + 10 min of exposure to laser illumination at 3 w/cm^2 (photothermal treatment) and Fe$_3$O$_4$@Au@mSiO$_2$-dsDNA/DOX + 10 min of laser irradiation (combination therapy: photothermal + chemotherapeutic treatments) were performed, resulting in the cell survival rates as 83% and 49%, respectively, suggesting better therapeutic effects with the combination therapy than with the photothermal treatment alone. It is noted that better therapeutic effects were observed when magnetic attraction was applied for a period of 2 h. Due to more cell-uptake of NPs by the magnetic attraction, the significant drops of cell survival were down to 65% and 34% for Fe$_3$O$_4$@Au@mSiO$_2$-dsDNA + 2 h of magnetic attraction +10 min exposure of laser illumination (photothermal treatment) and Fe$_3$O$_4$@Au@mSiO$_2$-dsDNA/DOX + 2 h of magnetic attraction +10 min of laser illumination (combination therapy), respectively. In addition, a DOX alone group was added to the cells, wherein the concentration of DOX was the same as that carried by NPs, and the resulting cell survival was 78%. These results indicate the effective efficacy from the combination therapy as well as the synergistic effect from the application of the magnet.

Figure 6b shows the laser confocal fluorescence microscopy conducted on monitoring drug release and cells imaging. In the control group (cells alone), the complete cytoskeletons and full cell nuclei were clearly visible. In the other groups, with the presence of Fe$_3$O$_4$@Au@mSiO$_2$-dsDNA/DOX, all images were taken to reveal the therapeutic effect of the combination therapy. Two experimental conditions were performed for the cells with Fe$_3$O$_4$@Au@mSiO$_2$-dsDNA/DOX. In one condition, the images were captured immediately after 10 min of laser illumination at 808 nm diode laser (3 W/cm^2) following 2 h of culturing (without magnet attraction) with the addition of 400 ppm (of Au concentration) of Fe$_3$O$_4$@Au@mSiO$_2$-dsDNA/DOX. In the other condition with magnetic attraction added during 2 h of culturing, the images were taken immediately after the laser irradiation. In both performances, with or without the magnet application, for the cell images taken immediately after laser illumination, incomplete segments of cell membrane were observed and the cell nuclei had experienced pyknosis, which is a sign of cell apoptosis. The red fluorescence (i.e., the presence of DOX) was detected in cytoplasm, suggesting drug release after laser illumination. In the case of the group with magnetic attraction, the more distinct red fluorescence came from the drugs the more significant damage to the cells were observed. To observe the effect of anticancer DOX on the cells, the experiments mentioned above were repeated but the images were not taken immediately but with additional 24 h of incubation after the laser illumination. An encouraging result was discovered that for all groups, regardless having the application of magnetic attraction or not, a greater degree of cell damage was observed than that found in the studies of "immediately after laser irradiation". Particularly in the group with magnetic attraction, the cytoskeletons experienced severe damage and pyknosis of nuclei was evident. Also, the red fluorescence of the DOX was concentrated in the nuclei (coexistence of red and blue fluorescence). It is clearly that the drug had penetrated the nuclei and taken effects, thus causing
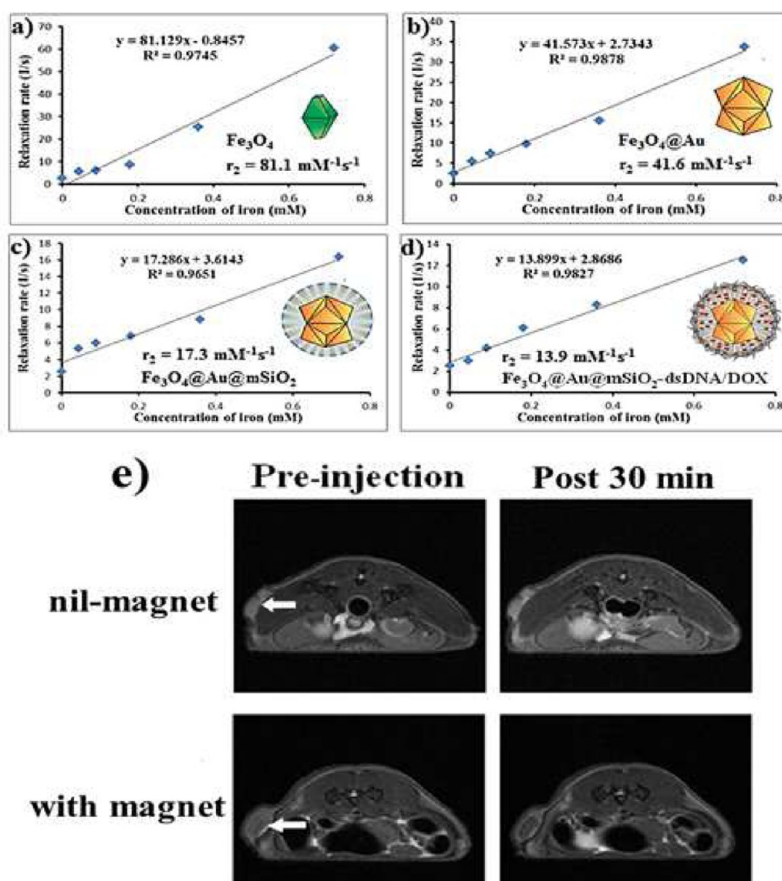
10069

dx.doi.org/10.1021/ja504118q | *J. Am. Chem. Soc.* 2014, 136, 10062−10075

Figure 8. The r_2 values of (a) Fe_3O_4, (b) $Fe_3O_4@Au$, (c) $Fe_3O_4@Au@mSiO_2$, and (d) $Fe_3O_4@Au@mSiO_2$-dsDNA/DOX NPs were calculated by T_2 relaxation ($1/T_2$, s^{-1}) rate versus iron concentration. (e) The T_2-weighted images of $Fe_3O_4@Au@mSiO_2$-dsDNA/DOX were monitored using a 9.4 T animal micro MRI system as the NPs were administrated by intravenous injection of 0.55 mg DOX/kg. The images were captured of preinjection and postinjection at 30 min. Control group (without magnetic guiding) and the group with the magnet guiding for 30 min after particles administration. White arrows indicate the location of tumor.

damage to the cells. To demonstrate DOX release controlled by laser irradiation, two additional cell images with $Fe_3O_4@Au@mSiO_2$-dsDNA/DOX NPs were presented in the absence of laser illumination. Images taken immediately after 2 h of magnetic attraction and additional 24 h of incubation after 2 h of magnetic attraction all show little red fluorescence of DOX appeared in the cells. These results further verify the DOX release upon laser irradiation.

We extended the studies from *in vitro* to *in vivo* to investigate the regression efficacy in tumor growth, which was monitored in terms of tumor volume change (Figure 7). HeLa cells were transplanted hypodermically in the thighs of the nude mice. Forty-five nude mice bearing HeLa tumors were divided into nine groups. The mice were injected through a tail vein with NPs at a fixed dosage of ~0.55 mg DOX/kg corresponding to a 6.5×10^4 ppm Au/kg. For the experiments under the magnetic attraction, the magnet attraction was applied for 30 min along with NPs injection. The laser exposure was conducted using an 808 nm diode laser for 30 min of irradiation at 3 W/cm². For the groups treated with PBS only, PBS + laser illumination, and $Fe_3O_4@Au@mSiO_2$-dsDNA NPs + magnet attraction, the mice were closely monitored for the continuous growth of tumor, which grew 7 times larger on day 14 than it was initially. In the cases of DOX only, $Fe_3O_4@Au@mSiO_2$-dsDNA/DOX + magnet attraction, $Fe_3O_4@Au@mSiO_2$-dsDNA/DOX + laser illumination, and $Fe_3O_4@Au@mSiO_2$-dsDNA + magnet

attraction + laser illumination, minor suppression of the tumors was seen as the tumors grew 5−6 times larger after 14 days. Contrarily, when the magnetic attraction was applied, followed by laser illumination for the group of $Fe_3O_4@Au@mSiO_2$-dsDNA/DOX + magnet attraction + laser illumination, the tumor grew only 3 times larger in 14 days. This indicates that the focus of the magnetic target for NPs at the tumor along with laser illumination resulted in the effectiveness of combination treatment and suppression of tumor growth. Finally, if the second dose was administered on day 5 with the same 30 min of magnetic attraction and 30 min of laser illumination, it was encouraging to see that the tumor disappeared completely after 14 days. Figure S14 shows the biodistribution after injection of $Fe_3O_4@Au@mSiO_2$-dsDNA/DOX NPs into mice bearing HeLa tumors through a tail vein with or without 30 min of magnetic targeting. The tissues were surgically removed after 30 min and 24 h of injection. Heart, liver, kidneys, spleen, and tumor tissues were taken and subjected to ICP-AES analysis to determine quantitatively the contents of NPs in these tissues. In comparison, the enhanced amount of NPs accumulated at the tumor in the group with the magnetic attraction, as opposed to <10% of that observed in the tumors of the group without magnetic attraction. The attraction of external magnetic field contributed to the accumulation of sufficient NPs in the tumor and thus improved the effect of subsequent treatments. In the group with magnetic attraction,

NPs were mainly distributed in the liver, spleen, and tumor tissues. After 24 h postinjection, NPs approximately retained the same amount in the tumor. On the other hand, the significant amount NPs revealed a dominant uptake in the liver at initial 30 min in the group without magnetic attraction and then were gradually eliminated as time progressed to 24 h. Considering the toxic evaluation, we have monitored liver function indices (ALP, AST, ALT, and T-Bil) for blood analysis (Figure S15). These indices have been widely used to determine whether there is inflammation in liver. Following the same experimental conditions in biodistribution with the presence of magnetic attraction for 30 min at the tumor site along with NPs injection, the samples were taken at 30 min, 24 h, and 21 days after the injection of NPs. The results show no significant difference between the experiment group and control group injected with PBS. In addition, we resected and then dissected the organs of the heart, lung, liver, kidney, and spleen for histological analysis at 24 h, 7 days, and 21 days postinjection for any change in the morphology due to material toxicity (Figure S16). The tissues after hematoxyline and eosin staining showed well-organized cell structure as that of the control set. Especially the intact morphology of spleen, which plays an important role in blood purification, does not show any change in morphology due to absence of immune activity. With these preliminary toxicological results, it is believed that the current NPs proposed have no acute toxicity as a cancer medicine.

Finally, iron oxide NPs are a class of noninvasive imaging agents that have been developed for magnetic resonance (MR) imaging. They are known to show effective proton T_2 relaxation. Such a relaxation resulted in reduction in signal intensity, leading a visible MR image. MRI visibility has, thus, offered an opportunity to monitor NPs accumulation and to evaluate targeting effect in tumor site. The *in vitro* spin−spin relaxation time T_2-weighted imaging was evaluated by using 0.5% agarose gel for NPs. A series of different ion concentrations were investigated for the r_2 relaxivities, where the values were calculated from a plot of the relaxation rate versus the iron ion concentration (Figure 8a−d). In this study, the r_2 values were identified using the Minispec Contrast Agent Analyzer (1.4T), which was determined to be 81.1, 41.6, 17.3, and 13.9 mM^{-1} s^{-1} for Fe_3O_4, Fe_3O_4@Au, Fe_3O_4@Au@mSiO$_2$, and Fe_3O_4@Au@mSiO$_2$-dsDNA/DOX, respectively. Fe_3O_4@Au@mSiO$_2$-dsDNA/DOX was wrapped layer after layer and loaded with drugs, which caused an apparent reduction of r_2 value approximately 6-fold less than that of initial Fe_3O_4. However, the *in vivo* MR imaging revealed that the smaller r_2 value in Fe_3O_4@Au@mSiO$_2$-dsDNA/DOX still can work as an effective T_2 contrast agent. Once again, the mice were injected with HeLa cells hypodermically. The experiments were conducted after a week of tumor growth, and the tumor then was subjected to the measurements using a 9.4 T animal micro MRI system. The injection dosage was the same amount of Fe_3O_4@Au@mSiO$_2$-dsDNA/DOX used for *in vivo* therapeutic studies. When 30 min of magnetic attraction was applied after the injection of the NPs, apparent contrast change in signal was found in MR images. The quantitative analysis showed the contrast signal of tumor after magnetic attraction was reduced to 77.8% (Figure 8e). Contrarily, no contrast change in the tumor was seen for the group with injection of NPs, but without magnetic attraction. This indicates that once the Fe_3O_4@Au@mSiO$_2$-dsDNA/DOX was injected into mice's body, the manipulation by an external magnet caused the NPs

to accumulate at the tumor in large quantity in a fairly short period of time, which significantly improved the negative contrast effect at the tumor. Apart from confirming that Fe_3O_4@Au@mSiO$_2$-dsDNA/DOX is an effective MRI T_2 contrast agent, it also evident that the NPs can be used as an effective magnetic target.

CONCLUSIONS

Unlike previous Fe_3O_4@Au NPs exhibiting a spherical morphology, the truncated octahedral Fe_3O_4 NPs were used as the core over which a layer of trisoctahedral Au shell was generated. This new multifunctional nanoplatform was successfully demonstrated for the applications in the biomedical field. A layer of mSiO$_2$ shell was wrapped around the entire assembly to perform a NIR-responsive remote control drug release behavior. The modification of dsDNA was adopted as the switch for remote NIR control. As far as the research is concerned, we have created a multifunctional drug control and release carrier that features functions of magnetic target, MRI diagnosis, and combination therapy through manipulation by magnet attraction and NIR laser illumination. The results verified the significant therapeutic effects on tumors with the assistance of combination therapy consisting of magnetic guidance and remote NIR control. A preliminary material safety experiment was performed, and no permanent damage was found to the living organisms to which a high dosage of this NP was administered. For practical applications in the biomedical field, future work can be a more in-depth biological safety test. It is expected that a multifunctional NP featuring magnetic guidance, combination therapy, and diagnosis will provide a potent therapeutic choice in the biomedical field.

EXPERIMENTAL SECTION

Materials. All reagents were of analytical purity and used without further purification. L-ascorbic acid (AA, $C_6H_8O_6$, 99%), iron(III) acetylacetonate (Fe(C$_5$H$_7$O$_2$)$_3$, 99.9%), trioctylamine (TOA, [CH$_3$(CH$_2$)$_7$]$_3$N, 98%), oleic acid (OA, CH$_3$(CH$_2$)$_7$CH=CH-(CH$_2$)$_7$COOH, 90%),α,ω-bis{2-[(3-carboxy-1-oxopropyl)amino]-ethyl}polyethylene glycol (COOH-PEG-COOH, M_W: 6000), poy-L-lysine hydrobromide (PLL, L-Lys-(L-Lys)$_n$-L-Lys·xHBr, M_W: 1000−5000 and 500−2000), poly-L-histidine hydrochloride (PLH, L-His-(L-His)$_n$-L-His·xHCl, M_W: 5000), poly-L-arginine hydrochloride (PLA, L-Arg-(L-Arg)$_n$-L-Arg·xHCl, M_W: 5000−15000), polyethylenimine (PEI, (CH$_2$CH$_2$NH)$_n$, M_W: 5000) doxorubicin hydrochloride (DOX, $C_{27}H_{29}NO_{11}$·HCl, 98%), *para*-formaldehyde (HO(CH$_2$O)$_n$H, 95%), Hoechst 33342 ($C_{27}H_{28}N_6O$·3HCl·3H$_2$O, 98%), and 3-(4,5-dimethylthiazol-2-yl)-2,5-diphenyltetrazolium bromide (MTT, $C_{18}H_{16}BrN_5S$, 97.5%) were used as purchased from Sigma-Aldrich. 3-aminopropyl-ethoxysila (APTES, $C_8H_{23}NO_3Si$, 99%) and tetraethyl orthosilicate (TEOS, $C_8H_{20}O_4Si$, 98%) were purchased from ACROS. Hydrogen tetrachloroaurate (III) trihydrate (HAuCl$_4$·3H$_2$O, 99.99%) was obtained from Alfa Aesar. Sodium hydroxide (NaOH, 99%) was bought from FULLIN. Trisodium citrate dehydrate (HOC(COONa)-(CH$_2$COONa)$_2$·2H$_2$O, 99%) was used as purchased from SHOWA. Cetyltrimethylammonium chloride solution (CTAC, CH$_3$(CH$_2$)$_{15}$N-(CH$_3$)$_3$Cl, 25 wt%, in H$_2$O was purchased from Aldrich. Hydroquinone ($C_6H_6O_2$, 99.5%) was purchased from Riedel-deHaen. Hexadecyltrimethylammonium bromide (CTAB, CH$_3$(CH$_2$)$_{15}$N(Br)-(CH$_3$)$_3$, 96%) and N-γ-maleimidobutyryloxy succinimide (GMBS, $C_{12}H_{12}N_2O_6$, 98%) were purchased from Fluka. Chloroform (CHCl$_3$, 99.8%) was obtained from MERCK. Ethanol (C_2H_5OH, 99.9%), hexanes (C_6H_{14}, 99.9%), sodium chloride (NaCl, 99.6%), sodium dodecyl sulfate (SDS, $C_{12}H_{25}SO_4Na$, 100%), monopotassium phosphate (KH$_2$PO$_4$, 99.6%), dipotassium phosphate (K_2HPO_4, 100%), and sodium bicarbonate (NaHCO$_3$, 97.5%) were purchased from J.T.Baker. Alexa Fluor 488 phalloidin was used as purchased from

Invitrogen. Dulbecco's modified eagle medium (DMEM, high glucose, pyruvate), antibiotic-antimycotic (PSA), MEM nonessential amino acids solution (NEAA), and 0.25% trypsin-EDTA were bought from Gibco. Fetal bovine serum characterized (FBS) was used as purchased from HyClone. Water throughout all studies was generated by using a Millipore direct-Q deionized water system.

Preparation of Truncated Octahedral Fe_3O_4 NPs. The truncated octahedral Fe_3O_4 magnetic NPs were prepared using a method from the previous studies.[29] As an example, for the synthesis of 22 nm-sized NPs, 1.45 g of iron(III) acetylacetonate was added to 0.56 mL of oleic acid in 20 mL of trioctylamine at 150 °C for 1 h. The temperature was decreased to temperature of 120 °C, at which it was held constant for 1 h on vacuum environment. Next step, the temperature was increased at a rate of 2 °C/min to temperature of 305 °C, where it was held constant for 20 min. After cooling to room temperature, the precipitates were collected and washed using a toluene/ethanol (v/v =1:4) solution. After a centrifuging process, the supernatants were discarded, and the Fe_3O_4 NPs were then redispersed and stored in hexane.

Ligand Exchange of Truncated Octahedral Fe_3O_4 NPs. Exchange of the hydrophobic oleic acid surface ligands on Fe_3O_4 NPs for the hydrophilic ligands was carried out according to following procedures: 1 mL of Fe_3O_4 NPs solution was dried by oven and then was dispersed in 0.1 mL chloroform. The hydrophilic ligand (COOH-PEG-COOH, M_W: 6000) solution was prepared with a 4 mg of PEG in a 2 mL deionized water containing 2 mL of 2 M NaOH(aq). Next step, the iron oxide solution was added slowly. The hydrophilic Fe_3O_4 NPs were generated under the mixture sonicated for 4 h. After centrifugation at 14000 rpm for 10 min, the supernatants were discarded, and the pellets were then redispersed and stored in deionized water.

Preparation of Trisoctahedral Fe_3O_4@Au NPs. Trisoctahedral Fe_3O_4@Au NPs were generated by three steps. First, 0.1 mg of truncated octahedral Fe_3O_4 NPs was dispersed in 0.75 mL deionized water containing 0.75 mL of 0.4 mM PLL. And then, the sample was mixed by vortex for 24 h. Next step, 1.3 mL of 5 mM $HAuCl_4$ solution was dispersed in 5.2 mL deionized water, and then 0.01 M NaOH solution was used to adjust the pH value to about 10.9. The 1.5 mL of Fe_3O_4 solution and 0.1 mL of 0.038 mM trisodium citrate solution were added to the $HAuCl_4$ solution. The sample was mixed in a dark environment for 24 h. Finally, the reaction solution was transferred to a new flask under vigorous stirring. After for 2 min, 0.3 mL of 0.1 M L-ascorbic acid was injected for gold nanoshell formation, stirred for another 30 min, and then centrifuged at 2000 rpm for 8 min to collect NPs. The resulting Fe_3O_4@Au NPs were harvested by applying an external magnet to remove from the solution. The precipitates were then washed several times with deionized water and then dispersed in deionized water.

Preparation of Fe_3O_4@Au@$mSiO_2$ and Its Subsequent Modification. A colloidal solution of Fe_3O_4@Au NPs (1000 ppm in Au ion concentration) was added to the aqueous solution containing 0.5 mL of 0.1 M CTAB. After stirring for 5 min at 55 °C, NaOH solution (0.05 M, 0.25 mL) and TEOS (15 µL) were added to the solution. The reaction mixture was vigorously stirred at 55 °C for 4 h. Subsequently, the solution was centrifuged at 4500 rpm for 10 min to remove supernatant. The precipitates were washed with ethanol at least three times. Next step to modify APTES, as-synthesized Fe_3O_4@Au@$mSiO_2$ (1000 ppm in Au ion concentration) was redispersed in a solution containing 4 mL of ethanol and 5 µL of (3-aminopropyl)triethoxysilane (APTES) for reaction. After reaction for a day at room temperature, the particles were collected by centrifugation (11500 rpm, 15 min) and washed 3 times with ethanol. The precipitates (Fe_3O_4@Au@$mSiO_2$-APTES) were obtained. Subsequently, the resulting APTES-modified Fe_3O_4@Au@$mSiO_2$ colloids were dispersed in 4 mL of ethanol and 50 µL of 4-maleimidobutyric acid N-succinimidyl ester (GMBS, 22.5 mM) for reaction. After reaction for a day at room temperature, the solution was centrifuged at 11500 rpm for 15 min to remove supernatant. The precipitates were washed with ethanol at least three times. The precipitates (Fe_3O_4@Au@$mSiO_2$-APTES-GMBS) were obtained and dispersed in deionized water.

Hybridization of Double-Stranded Oligonucleotides (dsDNA). 6.2 µL of single-strand DNAs (100 µM) with a sequence of SH-5'-$(CH_2)_6$-TTTTTCCCGCGCCGG were hybridized with 6.2 µL of complementary single-strand DNAs (100 µM) with a sequence of 5'-TTTTTCCGGCGCGGG in 27.6 µL of PBS buffer containing 10 µL of 0.1% sodium dodecyl sulfate (SDS) at 4 °C for at least 10 min. The freshly prepared dsDNA was used for further experiments.

Preparation of DOX-Loaded Fe_3O_4@Au@$mSiO_2$-dsDNA (Fe_3O_4@Au@$mSiO_2$-dsDNA/DOX). 500 µL of as-synthesized Fe_3O_4@Au@$mSiO_2$-APTES-GMBS (100 ppm in Au ion concentration) was mixed with 100 µL of doxorubicin (DOX, 500 µM) in 350 µL of PBS buffer solution (10 mM) at room temp for 2 h, followed by addition of 50 µL of as-prepared dsDNA solution (100 µM) in PBS (10 mM, pH 7.4) buffer solution at 4 °C for reaction. After reaction for a day, the solution was centrifuged at 11500 rpm for 15 min to remove supernatant. The precipitates were washed with 10 mM PBS at least three times. The precipitates (Fe_3O_4@Au@$mSiO_2$-dsDNA/DOX) were obtained and redispersed in PBS buffer solution. The fluorescence intensity difference in DOX between the initial amount and residue in supernatants was performed to estimate the entrapped DOX concentration following a standard linear calibration curve based on the measurements of DOX fluorescence.

Preparation of FAM-Labeled Double-Stranded DNA-Modified Fe_3O_4@Au@$mSiO_2$. 6.2 µL of single-strand oligonucleotides (100 µM) with a sequence of SH-5'-$(CH_2)_6$-TTTTTCCCGCGCCGG was hybridized with 6.2 µL of complementary single-strand oligonucleotides (100 µM) with a sequence of FAM-5'-TTTTTCCGGCGCGGG (FAM:6-carboxy-fluorescine) in 27.6 µL of PBS buffer containing 10 µL of 0.1% sodium dodecyl sulfate (SDS) at 4 °C for at least 10 min. The freshly prepared FAM-labeled dsDNA was used for further experiments. 500 µL of as-synthesized Fe_3O_4@Au@$mSiO_2$-APTES-GMBS (100 ppm in Au ion concentration) was mixed with 50 µL of as-prepared FAM-labeled dsDNA solution (100 µM) in 450 µL of PBS (10 mM, pH 7.4) buffer solution at 4 °C for 24 h. After reaction, the solution was centrifuged at 11500 rpm for 15 min to remove supernatant. The precipitates were washed at least three times. The precipitates (Fe_3O_4@Au@$mSiO_2$-dsDNA-FAM) were obtained and redispersed in PBS buffer solution. The fluorescence intensity difference in FAM-labeled DNA between the initial amount and residue in supernatants was performed to calculate the quantity of dsDNAs attached to NP following a standard linear calibration curve based on the measurements of FAM-labeled DNA fluorescence.

Preparation of Au Nanospheres. The fresh Au seeds solution was prepared as follows. 28.5 mL of 5 mM $HAuCl_4$ solution was added to 28.5 mL deionized water in a flask. Then, the reaction flask was kept in an oil pot and heated at 120 °C. After 5 min, 1.22 mL of 38.8 mM citrate solution was added, and the heating was continued to 10 min. The color of the solution changed from light yellow to purple; this color change confirmed the formation of Au seeds.

We used hydroquinone as reducing agent for the growth of seed solution. First, we took 0.15 mL of fresh Au seeds solution and dispersed into 9 mL deionized water containing 0.6 mL of 5 mM $HAuCl_4$. Then the solution was allowed to stir at 5 min at room temperature. Finally, 30 µL of 38.8 mM citrate solution was added, followed by 0.1 mL of 0.03 M hydroquinone was injected for gold seed growth. 1 h aged solution showed the uniform size of spherical NPs. That solution was collected, then centrifuged at 4000 rpm for 10 min, the supernatants were discarded, and the centrifugate were redispersed into deionized water. We repetitively washed and centrifuged the nanomaterials at least three times. Finally, the trisoctahedral Au NPs were stored in deionized water.

Preparation of Au Nanotrisoctahedra. The trisoctahedral Au NPs were synthesized by an one-step process. The 0.64 mL of 0.78 M CTAC solution was taken and added into 94 mL deionized water containing 6 mL of 5 mM $HAuCl_4$. The solution was allowed to stir vigorously. Then when 1 mL of 0.1 M L-ascorbic acid was added, it acted as a reducing agent. After 1 h, the solution was collected,

10072

dx.doi.org/10.1021/ja504118q | J. Am. Chem. Soc. 2014, 136, 10062−10075

centrifuged at 4000 rpm for 10 min, the supernatants were discarded, and the pellets were redispersed into deionized water. We repetitively washed and centrifuged the nanomaterials at least three times. The trisoctahedral Au NPs were stored in deionized water.

Characterization of the NPs. Morphology of the colloids was monitored on the transmission electron microscopy (TEM, Hitachi H-7500). Structure of the polyhedral NPs was observed on high-resolution scanning electron microscope (HR-SEM, Hitachi SU8000). UV−vis spectra were recorded on a UV−vis absorption spectrometer (Hewlett-Packard Model 8453). X-ray diffraction signal of the NPs were obtained by the X-ray diffractometer (XRD, Shimasz Cu Kα radiation (λ = 1.54060 Å), 30 kV, 30 mA). Confocal microscope images were taken by laser scanning confocal microscope (Nikon inverted research microscope ECLIPSE Ti). Concentrations of the materials were measured by inductive coupled plasma atomic emission spectrometer (ICP-AES, Jobin Yvon JY138 Spectroanalzer). Magnetic properties of the NPs were detected by superconducting quantum interference device vibrating sample magnetometer (SQUID, Quantum Design MPMS). FT-IR spectrum of the NPs was observed on Fourier transform infrared spectrometer (FT-IR, JASCO 200E). A fluorescence spectrophotometer (PL, Hitachi F-2500) was used to measure the emission spectrum of fluorescent molecules. The BET specific surface area and the BJH pore volume and size distribution were determined by the nitrogen gas adsorption−desorption isotherms using a Micromeritics ASAP 2020 surface area and pore size analyzer. The quantification of cell viability was done using an enzyme-linked immune-sorbent assay reader (ELISA reader, Thermo Scientific Multiskan EX). T_2 relaxation rates were measured by a minispec contrast agent analyzer (Bruker Optik GmbH, mq60 system). The dynamic light scattering spectrometer (DLS, MALVERN Nano-ZS90) was used to measure the ζ potential of surface of NPs.

Stability Test for Fe$_3$O$_4$@Au@mSiO$_2$-dsDNA/DOX Without Laser Illumination. To confirm the stability of DOX in the porous, 200 μL of Fe$_3$O$_4$@Au@mSiO$_2$-dsDNA/DOX (50 ppm in Au ion concentration) in PBS (10 mM) contained in an eppendorf at 37 °C was monitored as a function of time. The liberated DOX was collected from the supernatant, and its concentration was calculated based on the fluorescence intensity by measuring the fluorescence emission of the DOX at 585 nm. The released DOX was calculated from a linear calibration curve (fluorescence intensity vs concentration).

In order to understand stability of dsDNA on the particles surface, original DNAs were replaced for the fluorescent FAM-labeled DNA. 200 μL of Fe$_3$O$_4$@Au@mSiO$_2$-dsDNA-FAM (50 ppm in Au ion concentration) in PBS (10 mM) was incubated in eppendorf at 37 °C and monitored as a function of time. The liberated FAM-labeled DNAs were collected from the supernatant, and its concentration was calculated based on the fluorescence intensity by measuring the fluorescence emission of the FAM at 518 nm. The released FAM-labeled DNAs were calculated from a linear calibration curve (fluorescence intensity vs concentration).

Temperature Elevation Profile by Photothermal Conversion. 100 μL of Fe$_3$O$_4$@Au and Fe$_3$O$_4$@Au@mSiO$_2$-dsDNA/DOX with different concentrations in PBS (10 mM) was added to the culture well of 96-well plates. The efficiency of photoinduced temperature increase of the solution was investigated under 3 W/cm^2 using a NIR diode laser (808 nm) for 15 min irradiation. The well was exposed to the laser light with a beam area of 0.13 cm^2. The change of temperature in solution was determined by a thermocouple coupled with a digital thermometer (TES 1319A−K type).

In Vitro Release of DOX Upon Laser Irradiation. 100 μL of Fe$_3$O$_4$@Au@mSiO$_2$-dsDNA/DOX (400 ppm in Au ion concentration) was placed in the culture well of 96-well plates. An ON-OFF switching sequence was operated, where the samples were exposed to NIR diode laser for 10 min and then unilluminated for 5 min. The solutions were centrifuged at 11000 rpm for 15 min, and the supernatants were collected to evaluate the released DOX by the measurements of fluorescence intensity. Once again, a standard linear calibration curve was performed to calculate the liberated DOX.

Cell Culture. HeLa cells (human cervical cancer cell lines) were cultured in DMEM containing 0.1 mM NEAA, 1% penicillin/

streptomycin (PS), and 10% FBS in the incubator at 37 °C and 5% CO$_2$.

In Vitro Cellar Uptake With or Without Magnetic Attraction. 5 ×10^3 HeLa cells/well were cultured in 96-well plates for 24 h, followed by treatment of Fe$_3$O$_4$@Au@mSiO$_2$-dsDNA/DOX (400 ppm in Au ion concentration) with or without magnet for 2 h. After that, the medium containing NPs was removed, and the cells well were washed with deionized water at least three times. Final, fresh aqua regia was added in the well for 24 h and then subjected to ICP-AES analysis.

In Vitro Cytotoxicity Studies of Fe$_3$O$_4$@Au@mSiO$_2$-dsDNA/DOX Nanoparticles Without Laser Illumination. MTT assays were carried out to quantify the cytotoxicity of Fe$_3$O$_4$@Au@mSiO$_2$-dsDNA/DOX NPs without laser irradiation. In the typical process, HeLa cells were cultured in 96-well plates (5 × 10^3 cells/well) for 24 h to allow the cells to be used. Subsequently, different concentrations of NPs were added to the culture medium. After 24 h incubation, the medium were removed, and cell culture was added with MTT reagent for 4 h, which was followed by the addition of DMSO to dissolve the purple crystals. Subsequently, the solution was centrifuged at 4000 rpm for 10 min to remove supernatant and then transferred to an ELISA plate. The quantification of cell viability was done using an ELISA plate reader. Eight repeats were done for each concentration group, and viability (%) was calculated by comparing cell viability in the absence of Fe$_3$O$_4$@Au@mSiO$_2$-dsDNA/DOX NPs.

In Vitro Cytotoxicity Studies of Fe$_3$O$_4$@Au@mSiO$_2$-dsDNA/DOX and Fe$_3$O$_4$@Au@mSiO$_2$-dsDNA With Laser Illumination. 5 ×10^3 HeLa cells/well were cultured on 96-well plates for 24 h, followed by the treatment of the Fe$_3$O$_4$@Au@mSiO$_2$-dsDNA/DOX or Fe$_3$O$_4$@Au@mSiO$_2$-dsDNA NPs (400 ppm in Au ion concentration). After 2 h incubation with or without magnet, the cells were washed twice with PBS and fed with fresh medium. For laser illumination, the cells were subjected to 3 W/cm^2 of NIR laser irradiation for 10 min. The cells were then incubated for another 24 h. For the cytotoxicity analysis the medium containing MTT reagent was added, and the cultures were incubated for 4 h to allow formazan dye to form. After this the MTT medium was removed, DMSO was added as a solvent, and cell viability was calculated based on the absorbance of purple formazan that was measured using ELISA plate reader.

Fluorescence Examination by The Laser Confocal Microscope. 1.2 × 10^4 HeLa cells/well were grown in medium at 37 °C in 5% CO$_2$ atmosphere in 8-well chamber slides for 24 h, followed by the treatment of the Fe$_3$O$_4$@Au@mSiO$_2$-dsDNA/DOX. After 2 h incubation with or without magnet, the adhered cells were gently rinsed twice to remove unattached NPs, and another fresh medium was added. The NPs-treated cells were then exposed to NIR diode laser (808 nm) with power density of 3 W/cm^2 for 10 min. After laser exposure, slides of cell samples were coverslipped immediately to monitor the effect of cell from photothermal ablation. On the orther hand, to monitor the combination therapy (photothermal and chemotherapeutic effects) for cells, additional 24 h incubation was performed after laser exposure, and then slides were coverslipped. For the coverslipped process, cells were rinsed twice and 100 μL of 4% para-formaldehyde was added to fix the cells for the observation. The cells were stained with Hoechst (nuclei, blue) and Alexa Fluor 488 phalloidin (cytoskeleton, green) after cells were perforated by Triton X-100. Finally, the slides were sealed, and the fluorescence images for prepared slides were taken with a laser scanning confocal microscope.

In Vivo Antitumor Efficacy of Fe$_3$O$_4$@Au@mSiO$_2$-dsDNA/DOX. All animal treatments and surgical procedures were performed in accordance with the guidelines of National Cheng Kung University (NCKU) Laboratory Animal Center (Tainan, Taiwan). All animals received humane care in compliance with NCKU guidelines for the maintenance and use of laboratory animals in research. All of the experimental protocols involving live animals were reviewed and approved by the Animal Experimentation Committee of NCKU. The antitumor efficacy of Fe$_3$O$_4$@Au@mSiO$_2$-dsDNA/DOX was evaluated using nude mice (BALB/cAnN), which was prepared by implanting subcutaneously the suspension of 6 × 10^6 HeLa cancer cells in medium (100 μL) into the right thigh of mice (5 weeks old; 17−20 g,

five mice per group). After 8 days of tumor xenografts, the tumor volume was approximately $100-150$ mm^3, and the tumor-bearing mice were ready for studies. The tumor size was measured along the longest width and the corresponding perpendicular length. The tumor volume was calculated using the volume of an ellipsoid, where volume = $4\pi/3$ (length/2 × width/2 × depth/2). This study assumed that depth = width and $\pi = 3$, resulting in volume = 1/2 × length × (width)^2.

On the groups without magnets, PBS solution, DOX solution, and Fe$_3$O$_4$@Au@mSiO$_2$-dsDNA/DOX were administrated by a intravenous injection at a DOX-equivalent dose of 0.55 mg/kg. After injection for 30 min, the mice tumor region was irradiated with a 808 nm diode laser at 3 W/cm^2 for 30 min. Mice tumor sizes were observed every 2 days.

On the experiment groups with magnets, Fe$_3$O$_4$@Au@mSiO$_2$-dsDNA or Fe$_3$O$_4$@Au@mSiO$_2$-dsDNA/DOX was administrated by a intravenous injection at a DOX-equivalent dose of 0.55 mg/kg corresponding to a 6.5×10^4 ppm Au/kg. The external magnetic field was applied for 30 min after injection. For laser illumination, the mice tumor region was irradiated with a 3 W/cm^2 808 nm laser for 30 min. Mice tumor sizes were observed by every 2 days.

Biodistribution Studies. Animals were sacrificed 30 min or 24 h after injection of Fe$_3$O$_4$@Au@mSiO$_2$-dsDNA/DOX with/without magnetic targeting 30 min. The tissues (heart, lung, liver, spleen, kidneys, and tumor) were collected, washed twice with normal saline solution, and stored in 4% *para*-formaldehyde solution. The samples were disrupted into powder by TissueRuptor (QIAGEN), and the powders were acid-digested in aqua regia for 1 week. The gold content of the samples was measured by ICP-AES. Three repeats were done for each group.

Evaluation of Magnetic Resonance Imaging. All animal treatments and surgical procedures were performed in accordance with the guidelines of Chang Gung Memorial Hospital Laboratory Animal Center (Kaohsiung, Taiwan). All animals received humane care in compliance with the institution's guidelines for maintenance and use of laboratory animals in research. All of the experimental protocols involving live animals were reviewed and approved by the Animal Experimentation Committee of Chang Gung Memorial Hospital Laboratory Animal Center. The diagnosis efficacy of Fe$_3$O$_4$@Au@mSiO$_2$-dsDNA/DOX was evaluated using nude mice (Nu/Nu), which was prepared by implanting subcutaneously the suspension of 6×10^6 HeLa cancer cells in medium (100 μL) into the right thigh of mice (6–8 weeks old; 25–30 g, three mice per group). After 8 days of tumor xenografts, the tumor volume was approximately $100-150$ mm^3, and the tumor-bearing mice were ready for studies. On the treatment, Fe$_3$O$_4$@Au@mSiO$_2$-dsDNA/DOX was administrated by the intravenously injection at a DOX-equivalent dose of 0.55 mg/ kg. The external magnetic field was applied for 30 min after injection (without magnet as sham control).

The tumor-bearing mice were anesthetized using 2% isoflurane (Abbott Laboratories, Abbott Park, IL) mixed with 100% O$_2$ delivered using a veterinary anesthesia delivery system (ADS 1000; Engler). Sequential MRI acquisitions were performed at a 9.4T MR imager (Bruker BioSpec 94/20 USR) equipped with a high-performance transmitter-receiver RF volume coil.

For T_2-weighted imaging, T_2-weighted axial anatomic reference imaging were recorded using multislice turbo rapid acquisition with refocusing echoes (Turbo-RARE) sequence acquisition at preinjection and 30 min postinjection (with/without magnetic guiding) with the following parameters: field of view = 35.0 × 35.0 mm; matrix dimension = 256 × 256 pixels; spatial resolution = 137 × 137 mm; slice thickness = 1.0 mm; echo time (TE) = 28.0 ms; repetition time (TR) = 3500 ms; rare factor = 4; refocusing flip angle = 180°; number of averages = 5; number of repititions (NR) = 1; total acquisition time = 9 min 20 s. The MR imaging signal intensities were measured using ImageJ 1.42 software and Matlab 6.0 software for Windows.

Blood Analysis of Fe$_3$O$_4$@Au@mSiO$_2$-dsDNA/DOX. Mice (n =3) were sacrificed 30 min, 24 h, and 21 days after the magnetic attraction for 30 min along with injection of Fe$_3$O$_4$@Au@mSiO$_2$-dsDNA/DOX. The mice blood was obtained from the heart, and then heparin sodium was added immediately. The clotted blood samples

were centrifuged at 1200 rpm for 15 min to obtain serum. The blood biochemistry analysis (ALP, AST, ALT, and T-Bil) was determined by biochemical analyzer (FUJI DRI-CHEM 4000i).

ASSOCIATED CONTENT

⑤ Supporting Information

The projection angles of trisoctahedron correspond to the Miller indices of high-index facets on an ideal crystalline model (Table S1). Additional TEM, HRTEM, ED, BET, BJH, FTIR, temperature elevation profile, the DOX release profile, and MTT assay. This material is available free of charge via the Internet at http://pubs.acs.org.

AUTHOR INFORMATION

Corresponding Author
csyeh@mail.ncku.edu.tw

Notes
The authors declare no competing financial interest.

ACKNOWLEDGMENTS

REFERENCES

(1) Habas, S. E.; Lee, H.; Radmilovic, V.; Somorjai, G. A.; Yang, P. *Nat. Mater.* **2007**, *6*, 692−697.

(2) Fan, F. R.; Liu, D. Y.; Wu, Y. F.; Duan, S.; Xie, Z. X.; Jiang, Z. Y.; Tian, Z. Q. *J. Am. Chem. Soc.* **2008**, *130*, 6949−6951.

(3) Yu, Y.; Zhang, Q.; Liu, B.; Lee, J. Y. *J. Am. Chem. Soc.* **2010**, *132*, 18258−18265.

(4) Wang, F.; Li, C.; Sun, L. D.; Wu, H.; Ming, T.; Wang, J.; Yu, J. C.; Yan, C. H. *J. Am. Chem. Soc.* **2011**, *133*, 1106−1111.

(5) Lu, C. L.; Prasad, K. S.; Wu, H. L.; Ho, J. A.; Huang, M. H. *J. Am. Chem. Soc.* **2010**, *132*, 14546−14553.

(6) Yang, C. W.; Chanda, K.; Lin, P. H.; Wang, Y. N.; Liao, C. W.; Huang, M. H. *J. Am. Chem. Soc.* **2011**, *133*, 19993−20000.

(7) Tsao, Y. C.; Rej, S.; Chiu, C. Y.; Huang, M. H. *J. Am. Chem. Soc.* **2014**, *136*, 396−404.

(8) Chiu, C. Y.; Huang, M. H. *Angew. Chem., Int. Ed.* **2013**, *52*, 12709−12713.

(9) Gong, J.; Zhou, F.; Li, Z.; Tang, Z. *Langmuir* **2012**, *28*, 8959− 8964.

(10) Hong, J. W.; Kim, D.; Lee, Y. W.; Kim, M.; Kang, S. W.; Han, S. W. *Angew. Chem., Int. Ed.* **2011**, *50*, 8876−8880.

(11) Kim, D.; Lee, Y. W.; Lee, S. B.; Han, S. W. *Angew. Chem., Int. Ed.* **2012**, *51*, 159−163.

(12) Kang, S. W.; Lee, Y. W.; Park, Y.; Choi, B. S.; Hong, J. W.; Park, K. H.; Han, S. W. *ACS Nano* **2013**, *7*, 7945−7955.

(13) Wang, L.; Bai, J.; Li, Y.; Huang, Y. *Angew. Chem., Int. Ed.* **2008**, *47*, 2439−2442.

(14) Zhai, Y.; Zhai, J.; Wang, Y.; Guo, S.; Ren, W.; Dong, S. *J. Phys. Chem. C* **2009**, *113*, 7009−7014.

(15) Goon, I. Y.; Lai, L. M. H.; Lim, M.; Munroe, P.; Gooding, J. J.; Amal, R. *Chem. Mater.* **2009**, *21*, 673−681.

(16) Xuan, S.; Wang, Y. X. J.; Yu, J. C.; Leung, K. C. F. *Langmuir* **2009**, *25*, 11835−11843.

(17) Gaytan, B. L. S.; Park, S. J. *Langmuir* **2010**, *26*, 19170−19174.

(18) Dong, W.; Li, Y.; Niu, D.; Ma, Z.; Gu, J.; Chen, Y.; Zhao, W.; Liu, X.; Liu, C.; Shi, J. *Adv. Mater.* **2011**, *23*, 5392−5397.

(19) Smolensky, E. D.; Neary, M. C.; Zhou, Y.; Berquo, T. S.; Pierre, V. C. *Chem. Commun.* **2011**, *47*, 2149−2151.

(20) Ji, X.; Shao, R.; Elliott, A. M.; Stafford, R. J.; Esparza-Coss, E.; Bankson, J. A.; Liang, G.; Luo, Z. P.; Park, K.; Markert, J. T.; Li, C. *J. Phys. Chem. C* **2007**, *111*, 6245−6251.

(21) Huang, H. C.; Tsai, P. J.; Chen, Y. C. *Small* **2009**, *5*, 51−56.

(22) Zhang, B. Q.; Ge, J.; Goebl, J.; Hu, Y.; Sun, Y.; Yin, Y. *Adv. Mater.* **2010**, *22*, 1905−1909.

(23) Xu, Z.; Hou, Y.; Sun, S. *J. Am. Chem. Soc.* **2007**, *129*, 8698−8699.

(24) Park, H. Y.; Schadt, M. J.; Wang, L.; Lim, I. S.; Njoki, P. N.; Kim, S. H.; Jang, M. Y.; Luo, J.; Zhong, C. J. *Langmuir* **2007**, *23*, 9050−9056.

(25) Larson, T. A.; Bankson, J.; Aaron, J.; Sokolov, K. *Nanotechnology* **2007**, *18*, 325101−325109.

(26) Fan, Z.; Shelton, M.; Singh, A. K.; Senapati, D.; Khan, S. A.; Ray, P. C. *ACS Nano* **2012**, *6*, 1065−1073.

(27) Levin, C. S.; Hofmann, C.; Ali, T. A.; Kelly, A. T.; Morosan, E.; Nordlander, P.; Whitmire, K. H.; Halas, N. J. *ACS Nano* **2009**, *3*, 1379−1388.

(28) Kim, J.; Park, S.; Lee, J. E.; Jin, S. M.; Lee, J. H.; Lee, I. S.; Yang, I.; Kim, J. S.; Kim, S. K.; Cho, M. H.; Hyeon, T. *Angew. Chem., Int. Ed.* **2006**, *45*, 7754−7758.

(29) Huang, C. C.; Chuang, K. Y.; Chou, C. P.; Wu, M. T.; Sheu, H. S.; Shieh, D. B.; Tsai, C. Y.; Su, C. H.; Lei, H. Y.; Yeh, C. S. *J. Mater. Chem.* **2011**, *21*, 7472−7479.

(30) Giri, S.; Trewyn, B. G.; Stellmaker, M. P.; Lin, V. S. Y. *Angew. Chem., Int. Ed.* **2005**, *44*, 5038−5044.

(31) Aznar, E.; Casasús, R.; García-Acosta, B.; Marcos, M. D.; Martínez-Máñez, R.; Sancenón, F.; Soto, J.; Amorós, P. *Adv. Mater.* **2007**, *19*, 2228−2231.

(32) Patel, K.; Angelos, S.; Dichtel, W. R.; Coskun, A.; Yang, Y. W.; Zink, J. I.; Stoddart, J. F. *J. Am. Chem. Soc.* **2008**, *130*, 2382−2383.

(33) Vivero-Escoto, J. L.; Slowing, I. I.; Wu, C. W.; Lin, V. S. Y. *J. Am. Chem. Soc.* **2009**, *131*, 3462−3463.

(34) Park, C.; Lee, K.; Kim, C. *Angew. Chem., Int. Ed.* **2009**, *48*, 1275−1278.

(35) Liu, R.; Zhang, Y.; Zhao, X.; Agarwal, A.; Mueller, L. J.; Feng, P. *J. Am. Chem. Soc.* **2010**, *132*, 1500−1501.

(36) Thomas, C. R.; Ferris, D. P.; Lee, J. H.; Choi, E.; Cho, M. H.; Kim, E. S.; Stoddart, J. F.; Shin, J. S.; Cheon, J.; Zink, J. I. *J. Am. Chem. Soc.* **2010**, *132*, 10623−10625.

(37) Luo, Z.; Cai, K.; Hu, Y.; Zhao, L.; Liu, P.; Duan, L.; Yang, W. *Angew.Chem. Int. Ed.* **2011**, *50*, 640−643.

(38) Chen, L.; Di, J.; Cao, C.; Zhao, Y.; Ma, Y.; Luo, J.; Wen, Y.; Song, W.; Song, Y.; Jianga, L. *Chem. Commun.* **2011**, *47*, 2850−2852.

(39) Perrault, S. D.; Chan, W. C. W. *J. Am. Chem. Soc.* **2009**, *131*, 17042−17043.

(40) Ma, Y.; Kuang, Q.; Jiang, Z.; Xie, Z.; Huang, R.; Zheng, L. *Angew. Chem., Int. Ed.* **2008**, *47*, 8901−8904.